AGU PUBLICATIONS

JGR

Journal of Geophysical Research: Space Physics

RESEARCH ARTICLE
10.1002/2017JA024523

Key Points:
- The 1-10 MeV electron dropouts at $L \sim 4.2$ turn out to be both more frequent and stronger than dropouts at 120-800 keV
- Results suggest an important role of precipitation loss due to combined EMIC and whistler mode waves in a large fraction of the events
- Almost all multi-MeV electron dropouts at $L \sim 4.2$ occurred above the plasmapause

Correspondence to:
R. J. Boynton,
r.boynton@sheffield.ac.uk

Citation:
Boynton, R. J., Mourenas, D., & Balikhin, M. A. (2017). Electron flux dropouts at $L \sim 4.2$ from Global Positioning System satellites: Occurrences, magnitudes, and main driving factors. *Journal of Geophysical Research: Space Physics*, *122*. https://doi.org/10.1002/2017JA024523

Received 27 JUN 2017
Accepted 28 OCT 2017
Accepted article online 6 NOV 2017

Electron Flux Dropouts at $L \sim 4.2$ From Global Positioning System Satellites: Occurrences, Magnitudes, and Main Driving Factors

R. J. Boynton[1], **D. Mourenas**[2], **and M. A. Balikhin**[1]

[1]Department of Automatic Control and Systems Engineering, University of Sheffield, Sheffield, UK, [2]CEA, DAM, DIF, Arpajon, France

Abstract Dropouts in electron fluxes at $L \sim 4.2$ were investigated for a broad range of energies from 120 keV to 10 MeV, using 16 years of electron flux data from Combined X-ray Dosimeter on board Global Positioning System (GPS) satellites. Dropouts were defined as flux decreases by at least a factor 4 in 12 h, or 24 h during which a decrease by at least a factor of 1.5 must occur during each 12 h time bin. Such fast and strong dropouts were automatically identified from the GPS electron flux data and statistics of dropout magnitudes, and occurrences were compiled as a function of electron energy. Moreover, the Error Reduction Ratio analysis was employed to search for nonlinear relationships between electron flux dropouts and various solar wind and geomagnetic activity indices, in order to identify potential external causes of dropouts. At $L \sim 4.2$, the main driving factor for the more numerous and stronger 1–10 MeV electron dropouts turns out to be the southward interplanetary magnetic field B_s, suggesting an important effect from precipitation loss due to combined electromagnetic ion cyclotron and whistler mode waves in a significant fraction of these events, supplementing magnetopause shadowing and outward radial diffusion which are also effective at lower energies.

1. Introduction

The outer radiation belt environment of the Earth consists of energetic electrons from ~100 keV to ~10 MeV, with flux levels that can vary by several orders of magnitude within a few hours (e.g., see Baker et al., 1986; Li et al., 2017; Turner et al., 2013) and pose various threats to satellites (Welling, 2010; Wrenn, 1995). Large and fast decreases in the electron population, called dropouts, have been investigated over more than a decade now, but the actual causes of such strong and fast electron losses throughout the outer radiation belt are not yet fully understood, in spite of some important advances (e.g., Green et al., 2004; Turner et al., 2013). Dropouts could be produced by a number of mechanisms, such as magnetopause shadowing aided by outward radial diffusion (Kim & Lee, 2014; Shprits et al., 2006; Turner et al., 2012; Ukhorskiy et al., 2015), precipitation loss (Bailey, 1968; Bortnik et al., 2006; Li et al., 2007; Mourenas et al., 2016; Su et al., 2016), or reversible adiabatic effects (Kim & Chan, 1997; McIlwain, 1966), either separately or simultaneously.

Magnetopause shadowing is due to the compression of the magnetopause by the solar wind. As the magnetopause moves closer to the Earth, the electrons that were on closed drift shells will be able to escape to open space. Once the magnetopause recovers to the precompression shape, there will be a higher electron Phase Space Density (PSD) closer to the Earth than farther away, where the electrons have just been lost. This spatial gradient in PSD then leads to a fast outward radial diffusion of electrons from the region of high PSD to the region where electrons have just been lost. This also results in a loss of electrons coming progressively closer to the Earth as electrons diffuse radially toward higher *L*s (Shprits et al., 2006; Turner et al., 2013).

Electron precipitation occurs due to resonant wave-particle interactions that scatter the electrons in pitch angle, ultimately leading to their loss into the upper atmosphere. The interaction of electrons with electromagnetic ion cyclotron (EMIC) waves (Li et al., 2007; Mourenas et al., 2016; Summers & Thorne, 2003), whistler mode chorus waves (Artemyev et al., 2016; Lorentzen et al., 2001; Mourenas et al., 2014; Orlova & Shprits, 2014), or hiss waves (Meredith et al., 2006; Mourenas et al., 2017), sometimes with a little help from fast magnetosonic waves (Balikhin et al., 2015; Mourenas et al., 2013), can cause pitch angle scattering loss.

The most rapid and important MeV electron dropouts of this kind are expected to be produced by simultaneous EMIC and whistler mode wave scattering (Mourenas et al., 2016, 2017; Zhang et al., 2017) and can occur for the average EMIC wave upper frequency cutoffs observed for H-band and He-band waves (Mourenas et al., 2016, 2017; Zhang et al., 2017), that is, such dropouts do not need EMIC waves very close to the helium gyrofrequency, contrary to dropouts due to EMIC waves alone. In the simultaneous presence of intense EMIC and chorus waves on the same L shell (possibly at different MLTs), whistler mode waves fill the trough in pitch angle diffusion at high equatorial pitch angles left by the sole EMIC wave diffusion. Moreover, EMIC wave scattering is so fast at low pitch angles that it creates a kind of effective loss cone for electrons at pitch angles much larger than the usual loss cone value, leading to a strong reduction of electron lifetimes as compared with a situation with whistler mode waves alone (without EMIC waves) (Mourenas et al., 2016, 2017; Zhang et al., 2017). Simulations have demonstrated that such combined diffusion by EMIC and whistler mode waves can really produce fast (<0.5–1 day) dropouts of electrons above ~2 MeV in realistic conditions, with MLT- and time-averaged EMIC wave amplitudes >50–100 pT and chorus amplitudes >50 pT (Mourenas et al., 2016, 2017; Zhang et al., 2017), even during nonstorm times (one such observation is discussed by Su et al., 2016).

Adiabatic effects result in a reversible loss of electrons due to the conservation of the three adiabatic invariants (Dessler & Karplus, 1961). During the main phase of a geomagnetic storm, the intensity of the ring current increases, decreasing the strength of the magnetic field, leading to the deceleration of electrons to conserve the first adiabatic invariant and the outward movement of the drift path to conserve the third adiabatic invariant. This is reversed when the ring current decreases back to its prestorm level, increasing the magnetic field strength, accelerating the electrons and moving back their drift paths closer to the Earth. Since this phenomenon occurs during geomagnetic storms, it has often been referred to as the "*Dst* effect" (Kim & Chan, 1997). Adiabatic effects should generally occur at all energies simultaneously and with similar strength. However, many past works have pointed out the importance of net electron flux loss during dropouts, demonstrating that reversible effects often do not prevail, at least around geosynchronous orbit (e.g., Boynton, Mourenas, et al., 2016; Turner et al., 2013).

Electron dropouts have mainly been studied at Geosynchronous Earth Orbit (GEO) due to the large amount of electron flux data available from the corresponding satellites. Borovsky and Denton (2010) used a superposed epoch analysis during geomagnetic storms to investigate the dropouts at GEO. They observed that increases in dynamic pressure and a southward interplanetary magnetic field (IMF) coincided with the dropouts. A superposed epoch analysis was also employed by Yuan and Zong (2013) for dropouts occurring during geomagnetic storms. They investigated the effects of solar wind dynamic pressure and different orientations of the IMF on the dropouts at GEO, showing similar results to Borovsky and Denton (2010), with high pressure and southward IMF leading to larger dropouts. Gao et al. (2015) studied all dropouts occurring during storm and nonstorm periods and found that both dynamic pressure and southward IMF can separately influence relativistic electron dropouts. They concluded that magnetopause shadowing was not responsible for all the dropouts. Boynton, Mourenas, et al. (2016) compiled statistical data of dropouts for energies ranging from 24 keV to 2.7 MeV and further determined the main solar wind and geomagnetic conditions controlling the dropouts, using a Nonlinear AutoRegressive Moving Average eXogenous (NARMAX) Error Reduction Ratio (ERR) approach. A minimum dropout by at least a factor of 4 was selected to differentiate dropouts from the slower electron flux decay due to scattering by chorus waves, since Boynton et al. (2014) had found that GEO electron fluxes decay slower (have lifetimes that increase) with increasing energy in rough agreement with chorus-induced electron loss models from Mourenas et al. (2012) at low energies. The ERR results showed that the factors having the most important influence on the dropouts were the *AE* index at low energies ($E \leq 90$ keV), dynamic pressure coupled with solar wind density at intermediate energies ($128 \leq E \leq 925$ keV), and dynamic pressure coupled with southward IMF at higher energies ($1.3 \leq E \leq 2$ MeV). They concluded that magnetopause shadowing coupled with outward radial diffusion is probably not the sole driving factor for all the dropouts, especially at MeV energies.

The aim of the present study is to investigate electron flux dropouts within the heart of the radiation belts at $L \sim 4.2$, for energies ranging from 120 keV to 10 MeV, and to try to identify their possible causes. Similar to Gao et al. (2015) and Boynton, Mourenas, et al. (2016), we compile a statistics of all dropouts occurring during both storm and nonstorm periods, using here 16 years of nearly equatorial electron flux measured on board the U.S. Air Force's Global Positioning System (GPS) satellites at $L \sim 4.2$. The electron flux data and the adopted criteria

for dropout selection are discussed in section 2. The statistical analysis of the dropouts is provided in section 3 and focuses on waiting times between dropouts and dropout magnitudes. Section 4 is devoted to a search for possible relationships between dropout magnitude and external factors, such as solar wind parameters and geomagnetic indices, making use of the NARMAX ERR methodology, which is able to determine the main controlling factors among various potential nonlinear relations (Boynton, Balikhin, Billings, Wei, et al., 2011; Boynton et al., 2013). The statistical results at $L \sim 4.2$ are then discussed in this light. Section 5 discusses the radial extension of dropouts of relativistic electrons, comparing the identified dropouts at $L \sim 4.2$ to dropouts at GEO catalogued by Boynton, Mourenas, et al. (2016). Finally, section 6 investigates the relationship of GPS dropouts with plasmapause and magnetopause locations.

2. Electron Flux Data and Methodology

The electron flux data used in this study come from the Combined X-ray Dosimeter (CXD) carried on board nine GPS Block IIR and IIR-M satellites designated as SVN53-61. All these spacecraft have a nearly circular orbit at an altitude of ~20,200 km with an inclination of 55° and, therefore, measure electron fluxes through a range of L shells at $L \geq 4.2$. The CXD instruments were designed at Los Alamos National Laboratory (LANL) over the course of more than 20 years. The electron flux data are supplied by the National Oceanic and Atmospheric Administration (NOAA) (https://www.ngdc.noaa.gov/stp/space-weather/satellite-data/satellite-systems/gps/), which provides differential electron fluxes at 15 energies from 120 keV to 10 MeV. The data are available from satellite SVN54 from February 2001 onward, eight other satellites having been added on GPS orbit over the following 7 years. These GPS data were made freely available to the scientific community thanks to the Executive Order "Coordinating Efforts to Prepare the Nation for Space Weather Events" issued by the White House on 13 October 2016. The corresponding data have been discussed in details by Morley et al. (2017). GPS electron fluxes have been checked to be similar (within a factor 2) to fluxes measured by the Van Allen Probes between 140 keV and 4–5 MeV (Morley et al., 2016).

This study aims to investigate dropouts in whole populations of electrons up to high equatorial pitch angles at $L \approx 4.2$ over a wide energy range. It is well known that all radiation belt electrons travel through the geomagnetic equator, whereas only part of them reach high geomagnetic latitudes. Therefore, for each energy range, the electron flux from each individual satellite was sampled when the spacecraft was at $4.1 < L < 4.3$ measuring electron fluxes in the vicinity of the geomagnetic equator. The data from all the satellites were then averaged over each 12 h period (00-12 UTC and 12-24 UTC), resulting in an electron flux data set from 18 February 2001 to 31 December 2016 for 15 energies with a 12 h cadence.

As for the previous study by Boynton, Mourenas, et al. (2016), an electron flux dropout is defined here as a flux decrease by a factor of 4 occurring over 1 day or less. Since our present GPS data set has a 12 h resolution, the dropout can take place over one or two time steps. The selection criteria of a decrease by factor of 4 were chosen so that the slower decay of electrons due to scattering by chorus or hiss waves, which usually corresponds to lifetimes >1 day for >120 keV electrons at $L \sim 4.2$ (e.g., Mourenas et al., 2014, 2016; Orlova & Shprits, 2014), would not be considered as a dropout. Therefore, the dropouts were defined as follows: (1) A decrease by a factor of 4 in 12 h (the previous electron flux, $J(t-1)$, being 4 times greater than the current flux, $J(t)$, $4J(t-1) \geq J(t)$); (2) A decrease by a factor of 4 in 24 h (the electron flux measured 2 time steps before, $J(t-2)$, being 4 times greater than the current flux, $J(t)$, $4J(t-2) \geq J(t)$) where there is a decrease by at least a factor of 1.5 in 12 h (the electron flux measured 2 time steps before, $J(t-2)$, being 1.5 times greater than the previous flux, $J(t-1)$, $1.5J(t-2) \geq J(t-1)$ and the previous electron flux, $J(t-1)$, being 1.5 times greater than the current flux, $J(t)$, $1.5J(t-1) \geq J(t)$).

The GPS electron flux data contain a number of spikes, or large and rapid oscillations, where the flux increases sharply before immediately strongly decreasing. Under the above-stated conditions, such peculiar oscillation events would have been counted as dropouts. However, the actual dropouts that we wish to study here rather correspond to periods of sudden, important loss occurring from an elevated, relatively stable level of electron flux, that is, not just rapid oscillations related, for instance, to narrow patches of high electron flux occasionally passing by the satellites. Therefore, two new conditions were added to remove such oscillation events. Such events were removed from the dropout list if (1) the electron flux 12 h before the start of the dropout, $J(t_B-1)$, was at least 2.5 times smaller than the electron flux at the start of the dropout, $J(t_B)$ $((2.5 * J(t_B - 1) \leq J(t_B))$.

Table 1
Number of Dropouts Observed Between 18 February 2001 and 31 December 2016 With the Variance of the Logarithmic Electron Flux

Energy	No. of Dropouts	Variance $\sigma_{\log J}$
120 keV	135	0.9973
210 keV	66	1.029
300 keV	42	1.078
425 keV	37	1.119
600 keV	33	1.011
800 keV	23	0.8265
1 MeV	33	0.7265
1.6 MeV	62	0.7558
2 MeV	92	0.9014
3 MeV	146	1.334
4 MeV	189	1.496
5 MeV	195	1.315
6 MeV	168	0.9954
8 MeV	133	0.7787
10 MeV	127	0.7622

(2) the electron flux 24 h before the start of the dropout, $J(t_B-2)$, was at least 4 times less than the electron flux at the start of the dropout, $J(t_B)$ ($(4 * J(t_B - 2) \leq J(t_B))$).

3. Statistical Analysis

3.1. Mean Waiting Time Between Consecutive Dropouts and Dropout Magnitudes

For each of the 15 energy channels, electron flux dropouts at $L \approx 4.2$ were automatically identified and some of their statistical properties were evaluated. Table 1 shows the number of dropouts identified for each electron energy channel within the 16 year period. One finds a low number of dropouts between 300 keV and 1 MeV, with only 23 to 42 dropouts observed in each of these energy channels over 16 years. Above 800 keV, the number of dropouts increases strongly, peaking at 5 MeV with 195 observed dropouts, then weakly decreasing up to 10 MeV. The low number of dropouts between 300 keV and 800 keV could stem from smaller flux variations in this range compared to other (higher or lower) energies. However, the global variance of the logarithmic electron flux does not show any relationship with the number of dropouts (see Table 1). As an example, Figure 1 displays the variations of 800 keV and 8 MeV electron fluxes over 16 years, which correspond to similar logarithmic variances, and where identified dropouts are marked in red. The much more numerous dropouts identified at 8 MeV simply correspond to 1 day periods during which the electron flux decreases sensibly faster than at 0.8 MeV. It is also worth emphasizing that for 30% to 40% of the identified dropouts at all energies, the electron flux does not recover a level comparable to its initial level before the dropout until at least 2–3 days after the dropout. In addition, the most numerous multi-MeV electron dropouts often occur several days after an important flux increase (see Figure 1), which may be due to chorus-induced electron acceleration during the recovery phase of a previous geomagnetic storm (Horne et al., 2005). Previous studies have shown that most electron flux dropouts at 1–3 MeV near geostationary orbit likely correspond to real losses (Boynton, Mourenas, et al., 2016; Turner et al., 2013).

For each energy channel, the corresponding mean waiting time between two successive dropouts (an important quantity for the determination of time-integrated radiation doses on satellites) was calculated as well as the 10, 20, 30, 40, 50, 60, 70, 80, and 90 percentiles of the distribution. The mean and percentiles are displayed in Figure 2 and are listed in Table 2. The mean waiting time increases with energy from 120 keV up to 800 keV

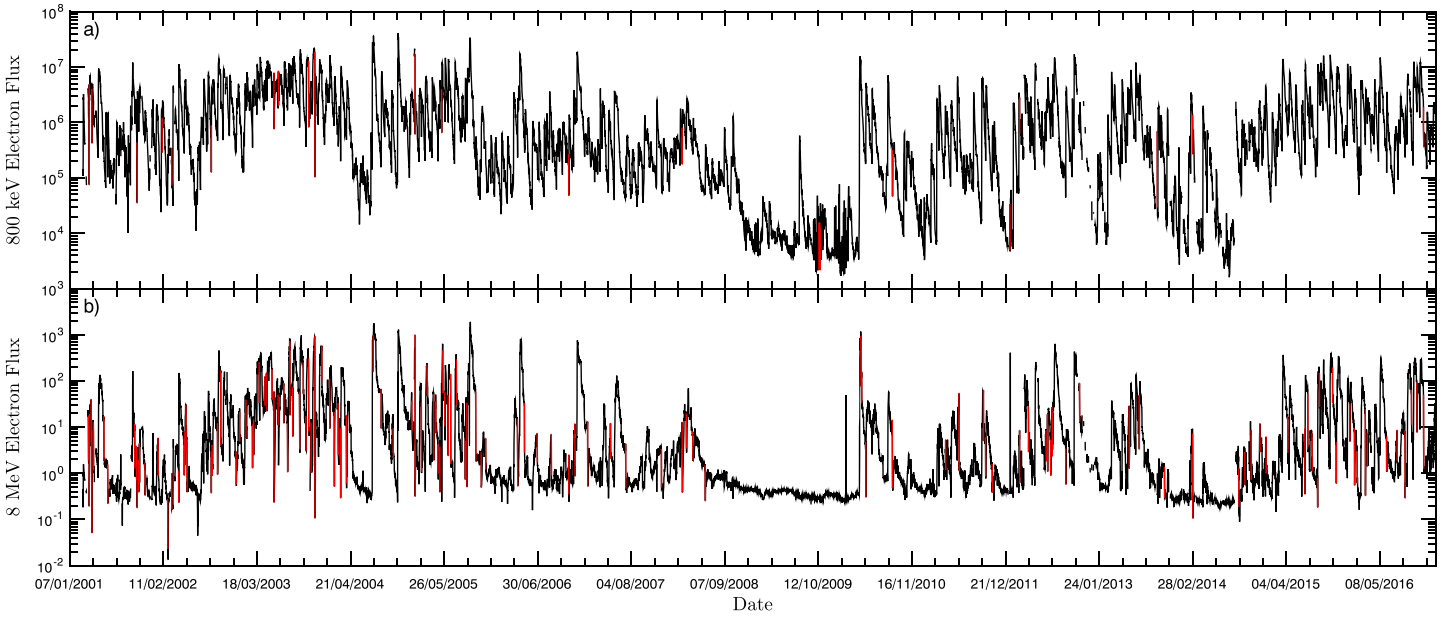

Figure 1. (a) The 800 keV electron flux and (b) the 8 MeV electron flux with the dropouts highlighted in red.

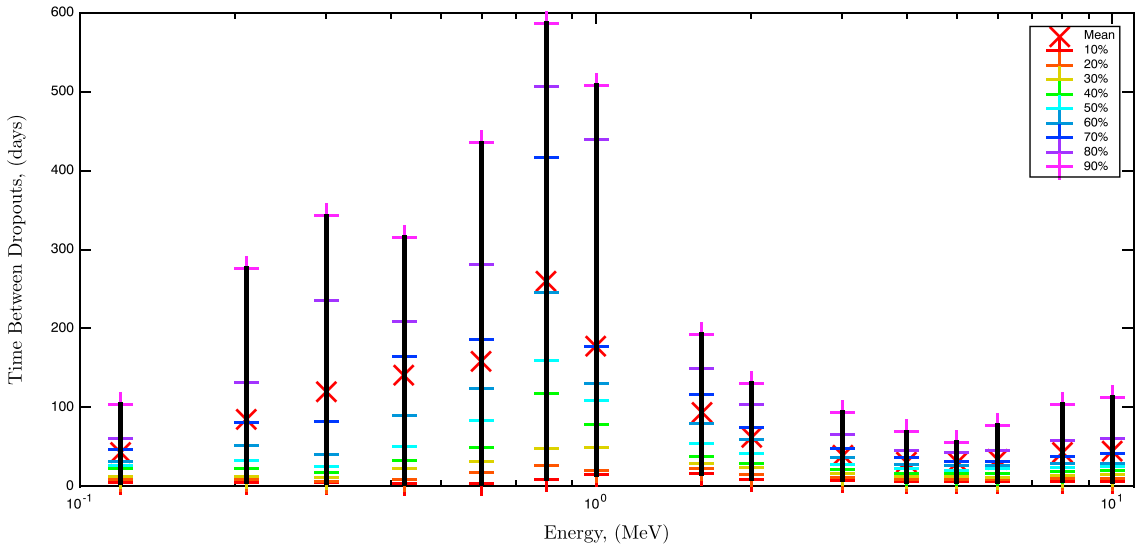

Figure 2. The mean waiting time between consecutive dropouts for each of the 15 energies (black cross) along with the 10 (red), 20 (orange), 30 (yellow), 40 (green), 50 (cyan), 60 (light blue), 70 (dark blue), 80 (purple), and 90 (magenta) percentiles of the distribution.

and then decreases, being sensibly smaller at 2–10 MeV than at 0.2–1 MeV. The percentiles show a similar pattern to the mean, where the mean is usually located around the 60–70 percentiles.

The mean and 10, 20, 30, 40, 50, 60, 70, 80, and 90 percentiles of the magnitude of the dropouts were calculated for each energy channel. The dropout magnitude was defined as the magnitude of electron flux decrease, given by the ratio $J(t_B)/J(t_D)$ of the flux at the time before the dropout, t_B, divided by the flux at the time of the dropout, t_D. The mean and percentiles are listed in Table 3 and shown in Figure 3. The mean dropout magnitude increases strongly with energy until 3 MeV and then oscillates. The median (50 %) dropout magnitude (as well as all percentiles above 30 %) exhibits a similar behavior as the mean, increasing with energy until 1 MeV and then remaining approximately constant, which implies that dropout magnitudes are globally increasing with energy. Both the 80 and 90 percentiles of dropout magnitudes are sensibly larger (by factors >2) at $E \geq 0.8$ MeV than at 0.12–0.6 MeV. Moreover, the mean is larger than the 90 percentile above 1 MeV, indicating the presence of a small number of extremely large dropouts in each of these high energy channels.

Table 2
Table Showing the Mean Waiting Time (in days) Between Dropouts for Each of the 15 Energies Along With the 10, 20, 30, 40, 50, 60, 70, 80, and 90 Percentiles of the Distribution

Energy	Mean	10%	20%	30%	40%	50%	60%	70%	80%	90%
120 keV	42.91	4.8	8.85	12.5	22	27	31.6	46.7	61.1	103.7
210 keV	84.91	5.5	8.2	13	22.85	33	52.15	80.3	131.6	275.9
300 keV	119.7	4.75	6.5	11.25	17.75	24.75	40.75	82.75	236	342.8
425 keV	140.9	3.25	9.25	22.95	32.25	50.75	90.3	164.7	208.9	315.7
600 keV	158.5	3.7	18.1	31.65	49.7	83.75	123.8	185.5	280.8	435
800 keV	259.2	9.25	26.2	48.1	118	160	245.5	416.5	506.6	585.7
1 MeV	178.2	15	20.35	49.65	78.1	109	129.7	177.1	440	508.2
1.6 MeV	93.5	16.5	22.75	29.3	38.4	54.5	80.2	116.6	149.2	192.7
2 MeV	62.68	9.3	14.95	23.5	29.4	41.5	58.75	75.1	103.8	129.7
3 MeV	40.07	7.8	11.5	16.9	21.85	27.5	37.15	48.1	65.45	93.3
4 MeV	30.81	6	8.5	12	16.45	23	27.5	36.5	45.6	69
5 MeV	29.99	6.35	8.5	12	16	20	25.85	31	43.05	55.7
6 MeV	34.68	6.05	8.5	11.5	16.45	22.5	27	31.35	45.6	77
8 MeV	43.23	6.5	9.45	14.1	18.3	24.5	28.5	37.95	58.1	103.8
10 MeV	45.29	6.5	10.2	14.65	19.8	25	29.55	41.15	60.65	113

Table 3
Table Showing the Mean Magnitude of the Dropouts Per Day for Each of the 14 Energies, Along With the 10, 20, 30, 40, 50, 60, 70, 80, and 90 Percentiles of the Distribution

Energy	Mean	10%	20%	30%	40%	50%	60%	70%	80%	90%
120 keV	18.55	4.235	4.624	4.894	5.262	5.81	6.46	7.336	16.19	29.71
210 keV	14.55	4.183	4.286	4.664	4.919	5.185	5.773	6.802	17.85	34.39
300 keV	23.83	4.152	4.574	5.028	6.221	12	18.32	21.12	32.79	53.68
425 keV	341.8	4.292	5.002	7.286	17.33	20.72	23.12	38.21	48.68	98.94
600 keV	47.95	4.341	4.548	5.188	6.46	18.85	24.86	39.94	44.2	95.67
800 keV	259.3	5.047	12.26	16.3	20.09	31.76	40.76	46.37	99.48	546.6
1 MeV	604.8	4.474	5.447	11.29	18.64	24.29	26.3	32.9	174.4	376.8
1.6 MeV	3887	4.739	7.165	9.887	18.69	26.18	34.61	54.81	89.28	1548
2 MeV	2.669e + 04	5.413	8.067	15.64	19.32	24.48	33.53	51.94	97.63	339.8
3 MeV	3.97e + 05	4.849	8.532	15.08	20.34	27.14	37.59	75.26	190.7	663.8
4 MeV	1.599e + 05	5.521	6.899	14.75	19.74	26.92	39.01	66.6	146.7	658.5
5 MeV	5,686	5.529	7.793	14.48	18.63	25.74	33.28	53.82	115.7	757.7
6 MeV	1,564	5.182	6.332	11.46	17.97	23.28	34.93	49.17	99.68	566.3
8 MeV	6.962e + 04	4.63	6.242	10.61	16.51	24.69	31.12	42.56	73.68	261.7
10 MeV	4.295e + 04	4.657	6.159	10.23	17.04	23.64	30.21	41.33	70.18	262.8

The above results demonstrate that there are consistently more frequent and stronger dropouts at high energy $E > 0.8 - 1$ MeV than at lower energy, suggesting either an energy-dependent efficiency of the loss processes or the presence of additional (or different) loss processes at higher energy. We shall now proceed in the next section to a NARMAX ERR analysis of potential governing factors for dropouts, with the hope that the additional insight gained from such an analysis will help us to identify the causes of the observed dependence of dropout magnitude and occurrences on electron energy, among a wealth of different possible mechanisms.

4. Solar Wind and Geomagnetic Activity Influence on Dropouts

4.1. Solar Wind Data and ERR Analysis

The solar wind parameters and geomagnetic activity indices are supplied by the OMNI website (http://omniweb.gsfc.nasa.gov). The upstream measurements of the solar wind are taken by the Advanced Composition Explorer situated at L1, which gives readings ~30–90 min in advance. These data were further sampled

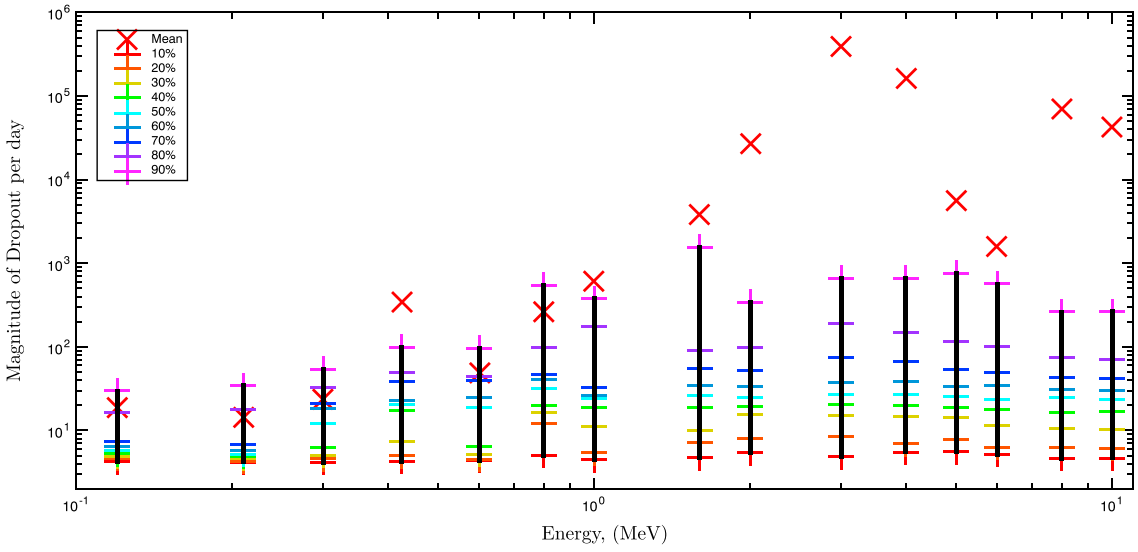

Figure 3. The magnitude of dropouts for each of the 15 energies (black cross) along with the 10 (red), 20 (orange), 30 (yellow), 40 (green), 50 (cyan), 60 (light blue), 70 (dark blue), 80 (purple), and 90 (magenta) percentiles of the distribution.

Table 4
ERR Analysis Results of the Dropout Factors, Where the Input Values Are the Solar Wind Velocity, Density, Dynamic Pressure, the Southward IMF B_s; the AE Index, and the Dst Index

Energy	1st Term	ERR	2nd Term	ERR	3rd Term	ERR
120 keV	$p(t-2)Dst(t-4)B_s(t-1)$	10.55	$Dst(t-4)B_s(t-1)n(t-2)$	1.508	$v(t-4)$	1.057
210 keV	$p(t-2)Dst(t-4)B_s(t-1)$	3.806	$Dst(t-4)AE(t-1)n(t-2)$	0.6786	$v(t-4)$	0.626
300 keV	$p(t-2)Dst(t-4)B_s(t-1)$	0.199	$Dst(t-1)V(t-4)$	0.08561	$v(t-0)$	0.05889
425 keV	$p(t-0)^2Dst(t-0)$	0.1808	$p(t-0)^2AE(t-0)$	0.0804	$n(t-0)$	0.05927
600 keV	$p(t-0)^2Dst(t-0)$	6.566	$B_s(t-1)^3$	5.235	$p(t-0)Dst(t-1)AE(t-0)$	2.982
800 keV	$B_s(t-1)^3$	36.71	$B_s(t-1)^2n(t-2)$	15.07	$p(t-0)^2Dst(t-0)$	10.1
1 MeV	$B_s(t-1)^3$	54.37	$B_s(t-1)^2n(t-2)$	22.48	$B_s(t-1)n(t-2)^2$	3.904
1.6 MeV	$B_s(t-1)^3$	61.08	$B_s(t-1)^2n(t-2)$	25.41	$B_s(t-1)n(t-2)^2$	4.342
2 MeV	$B_s(t-1)^3$	61.22	$B_s(t-1)^2n(t-2)$	25.5	$B_s(t-1)n(t-2)^2$	4.343
3 MeV	$B_s(t-1)^3$	61.24	$B_s(t-1)^2n(t-2)$	25.54	$B_s(t-1)n(t-2)^2$	4.345
4 MeV	$B_s(t-1)^3$	61.07	$B_s(t-1)^2n(t-2)$	25.44	$B_s(t-1)n(t-2)^2$	4.343
5 MeV	$B_s(t-1)^3$	61.27	$B_s(t-1)^2n(t-2)$	25.42	$B_s(t-1)n(t-2)^2$	4.383
6 MeV	$B_s(t-1)^3$	61.29	$B_s(t-1)^2n(t-2)$	25.39	$B_s(t-1)n(t-2)^2$	4.4
8 MeV	$B_s(t-1)^3$	61.1	$B_s(t-1)^2n(t-2)$	25.26	$B_s(t-1)n(t-2)^2$	4.406
10 MeV	$B_s(t-1)^3$	61.1	$B_s(t-1)^2n(t-2)$	25.19	$B_s(t-1)n(t-2)^2$	4.426

at a 12 h cadence to match the electron flux data over the same period of time from 18 February 2001 to 31 December 2016.

To identify the main external factors that influence the electron flux dropouts, this study employed a methodology based on the NARMAX ERR analysis (Billings et al., 1988; Boynton, Balikhin, Billings, Wei, et al., 2011). The ERR is able to identify a set of nonlinear parameters that control most of the variance of the output signal from input-output data and has previously been employed to identify the solar wind control parameters for the *Dst* index (Balikhin et al., 2010) and GEO electron fluxes in the radiation belt (Balikhin et al., 2012; Boynton et al., 2013). These control parameters were then successfully implemented as inputs to model the respective systems (Boynton et al., 2015; Boynton, Balikhin, Billings, Sharma, et al., 2011; Boynton, Balikhin, et al., 2016). The model structure used in this study can be represented mathematically as follows:

$$y(t) = F[u_1(t), u_1(t-1), \dots, u_1(t-n_{u_1}), \dots,$$
$$u_m(t), u_m(t-1), \dots, u_m(t-n_{u_m}), \dots, \quad (1)$$

where the output y at a time t is represented as a nonlinear function F, in the present case a polynomial, of m different inputs, each with a different maximum lag $n_{u_1}, \dots, n_{u_m}$. The terms with the highest ERR are more significantly contributing to the output variance. The advantage of the ERR analysis is that it is able to automatically identify and rank a wide class of nonlinear influences and separate out the contributions from the different governing factors.

For the ERR analysis, the output data were a time series of dropout magnitudes, defined as the electron flux before the dropout divided by the lower electron flux during the dropout. When no dropout was observed, dropout magnitudes were set to zero. The inputs were the solar wind velocity v, density n and dynamic pressure p, the southward IMF B_s, the *AE* index, and the *Dst* index. The minimum and maximum lags for the inputs were, respectively, set to 0 and 4 data points, the latter corresponding to 2 days in the past, and the nonlinear function F was assumed to be a third-order polynomial.

The results of the ERR analysis are listed in Table 4, which show the top three terms identified by the ERR analysis with their respective ERR. For energies ≤300 keV, $p(t-2)Dst(t-4)B_s(t-1)$ has the highest ERR, while between 425 keV and 600 keV, the term with the highest ERR is $p(t-0)^2Dst(t-0)$. One striking result of the analysis is that the term $B_s(t-1)^3$ turns out to have the highest ERR for all electron energies between 800 keV and 10 MeV. Moreover, the top three terms obtained from the ERR analysis are identical between 1 MeV and 10 MeV, with $B_s(t-1)$ appearing as the lone or dominant factor in the top two terms, whereas p and *Dst* are conspicuously absent from these three dominant terms. These results suggest that B_s is by far the main

governing factor for $E \geq 1$ MeV electron dropouts at $L \sim 4.2$, with no significant influence from solar wind dynamic pressure p or Dst, while p does play a role roughly equivalent to B_s or Dst in dropouts occurring at lower energy.

4.2. Discussion of Statistical Results in Light of the ERR Analysis

Below 700 keV, solar wind dynamic pressure p, Dst, and B_s at $E < 300$ keV appear as the prevalent factors determining dropout magnitudes. Unfortunately, the fact that all these different factors are similarly significant does not allow to discriminate between possible physical mechanisms. However, one very neat and important additional result of the ERR analysis is the identification of $B_s(t-1)^3$ as the main governing factor for dropout magnitude at high electron energy >0.8 MeV. The contrast with lower energies is striking. Clearly, B_s is considerably more important for dropouts at MeV and multi-MeV energy than it is at lower energy (compare the power of B_s in the dominant term and the presence of not of other factors in Table 4). Interestingly, although the $B_s(t-1)^3$ factor starts to become important at 0.6 MeV before prevailing above 0.8 MeV, the influence of solar wind dynamic pressure ($p(t-0)$) disappears only at slightly higher energy, for $E \geq 1$ MeV. This highlights the progressively more (less) prominent role played by B_s (p) as energy increases from 0.5 to 1 MeV.

Let us now reexamine our previous statistical results on dropout magnitudes and occurrences in light of the new information drawn from the ERR analysis. Figure 3 demonstrates that electron flux dropouts have a much stronger mean magnitude, and a sensibly higher median magnitude, at $E > 0.8$ MeV when the dominant driving term is $B_s(t-1)^3$ than at 120–600 keV where p, Dst, and B_s are similarly important. In contrast, the processes of magnetopause shadowing and subsequent outward radial diffusion are generally expected to be nearly independent of electron energy (e.g., Kim et al., 2008; Ozeke et al., 2014). Moreover, magnetopause shadowing can occur in the presence of either solar wind dynamic pressure impulses or strong B_s, with some simulations even suggesting that an increase in dynamic pressure p should lead to a stronger magnetopause shadowing than an increase of B_s (Kim & Lee, 2014; Kim et al., 2008). The fact that Dst has a significant impact on dropouts at 120–800 keV, but almost none at $E \geq 1$ MeV, further suggests that some identified dropouts might be partly related to a reversible Dst effect, but only (or mainly) in the range $E < 800$ keV.

A dominant effect of magnetopause shadowing (and outward radial diffusion) would therefore be consistent with both the roughly similar dropout magnitudes and occurrences at 300–600 keV in Figures 2 and 3 and the corresponding main controlling factors $p(t-0)^2 Dst(t-0)$ at 300–600 keV and $p(t-2)Dst(t-4)B_s(t-1)$ at 120–300 keV. At $E \leq 300$ keV, substorm-related electron injections can mitigate electron loss (Turner et al., 2017), probably explaining the weaker and less frequent dropouts in this low energy range. However, both the finding that the main (by far) governing factor at $E > 0.8$ MeV is $B_s(t-1)^3$ (i.e., with no dependence on p) and the sensibly larger magnitude and occurrence of dropouts in this high energy range do not seem to be consistent at all with a prevalence of magnetopause shadowing loss.

What could explain this apparent inconsistency? First, a dependence of the initial L distribution of the electron PSD on the first adiabatic invariant (i.e., on electron energy) could modulate the ultimate effects of magnetopause shadowing and outward radial diffusion on local flux variations. It is well known that important, localized PSD peaks usually form around $L \sim 5$–5.5 in the 1–5 MeV energy range, due to electron acceleration by chorus waves or inward radial diffusion from an on-off source (e.g., see Horne et al., 2005; Mann et al., 2016; Turner, Angelopoulos, Morley, et al., 2014). As a result, the initial electron PSD is generally decreasing faster between $L = 5$–5.5 and $L = 7$ in the multi-MeV energy range than at lower energy (Turner et al., 2013; Turner, Angelopoulos, et al., 2014). The initial $L \sim 4.2$ over $L = 7$ electron PSD ratio is then likely to be much higher at multi-MeV energies than at lower energy. A chorus-induced increase of electron PSD localized near $L = 5$ may therefore allow the formation of a steeper downward PSD gradient toward the magnetopause. Such a preconditioning can make the further development of a dropout via outward radial diffusion and magnetopause shadowing both easier and faster than for an initially null PSD gradient (Turner et al., 2013). All these facts could concur to produce stronger dropouts at multi-MeV energies than at 300–600 keV in the sole presence of significant magnetopause shadowing and outward radial diffusion. Deeper and more frequent dropouts at high energy could also occur due to drift shell bifurcation, which should lead to a larger spreading in L of particles and consequently a stronger loss at higher energy (e.g., Ozturk & Wolf, 2007; Ukhorskiy et al., 2015).

However, it is much more difficult to reconcile the assumption that magnetopause shadowing is the dominant cause of dropouts at MeV energies with the identification by the ERR analysis of B_s^3 as the sole main controlling factor of the magnitude of such dropouts, without any significant influence of solar wind dynamic pressure p. In the presence of magnetopause shadowing during strong IMF B_s, an increase of dropout efficiency might

Table 5
The Energy Channels at GEO, Equivalent Energy at $L \sim 4.2$ for the Same First Adiabatic Invariant, and the Corresponding GPS Energy Channels

Energy Channel at GEO (MeV)	Equivalent Energy at $L \sim 4.2$ (MeV)	Energy Channel on GPS (MeV)
0.4075	1.131	1
0.625	1.625	1.6
0.925	2.28	2
1.3	3.079	3
2	4.545	5
2.65	5.893	6

occur at high electron energy when there is an important *B* field gradient along the magnetopause, provided that there is no significant normal magnetic field component at the magnetopause, but this seems an infrequent situation (Kim & Lee, 2014). Moreover, it is unclear whether magnetopause shadowing, especially with a strong B_s alone and no dynamic pressure increase, can really manage to produce a strong and rapid dropout down to $L \sim 4.2$ (Gao et al., 2015; Kim & Lee, 2014; Kim et al., 2008; Turner, Angelopoulos, Morley, et al., 2014).

The preceding considerations suggest that fast dropouts of MeV electrons at $L \sim 4.2$ should be at least partly ascribed to some other (additional) physical processes, rather than to magnetopause shadowing and radial diffusion alone. But which other processes? Geomagnetic field line stretching near local midnight can lead to anomalous electron scattering at high (MeV) energies only, but this should work only during very strong storms (e.g., Artemyev et al., 2013; Sergeev & Tsyganenko, 1982).

Alternatively, dropouts can become stronger at relativistic energies due to MeV electron precipitation induced by combined effects of EMIC and chorus or hiss wave scattering (Li et al., 2007; Mourenas et al., 2016; Su et al., 2016; Zhang et al., 2017). In fact, EMIC and whistler mode wave amplitudes are known to increase strongly with geomagnetic activity, especially with *AE*, that is, not necessarily during storms (e.g., Artemyev et al., 2016; Kersten et al., 2014; Meredith et al., 2007, 2014; Mourenas et al., 2014, 2017; Orlova & Shprits, 2014; Zhang et al., 2016). Since *AE* is known to be influenced by the southward IMF B_s (e.g., Arnoldy, 1971; Meng et al., 1973), a larger B_s is expected to correspond to the presence of more intense EMIC and chorus waves. However, B_s was selected by the ERR analysis as a much more important parameter than *AE* for MeV electron dropouts. This could stem from a better correlation of the simultaneous presence of EMIC and chorus waves with B_s than with *AE*. Another explanation could be that most multi-MeV electron dropouts, being likely partly due to magnetopause shadowing, partly due to combined EMIC and chorus-induced loss, may better correlate with B_s variations. This would be consistent with a previous statistics of relativistic electron dropouts during both storm and nonstorm periods, based on Geostationary Operational Environment Satellites (GOES) and NOAA Polar Orbiting Environmental Satellites, which has shown that increases of B_s alone can indeed lead to strong dropouts coincident with intense MeV electron precipitation at $L \sim 3.5–5.5$ apparently linked to EMIC waves (Gao et al., 2015).

Therefore, the presence of some important MeV electron precipitation induced by simultaneous EMIC and whistler mode waves could really account for both the stronger mean (and, to a lesser extent, median) magnitude of dropouts observed at $L \sim 4.2$ for $E > 0.8$ MeV and the dominance of southward IMF B_s in the governing factors for such dropouts. Wave-induced precipitation could be dominant during only a small 10–20% portion of the multi-MeV dropouts, consistent with the mean and 80–90 percentiles of the dropout magnitudes being much higher than the median, but they could also contribute to the remaining dropouts, modulating the final dropout magnitude and blurring the influence of magnetopause shadowing and dynamic pressure *p*.

5. Radial Extension of Dropouts of Relativistic Electrons

To better assess the respective roles of magnetopause shadowing and precipitation in relativistic electron dropouts at $L \sim 4.2$, we can examine the radial extent of such dropouts. Are these GPS orbit dropouts extending up to GEO or not? Although precipitation loss related to EMIC waves may exist over a wide *L* range (e.g., Gao et al., 2015), wave statistics suggest its confinement to a domain of radial extension $\Delta L < 2$ in general (Usanova & Mann, 2016). Besides, GEO dropouts at relativistic energies often correspond to true losses

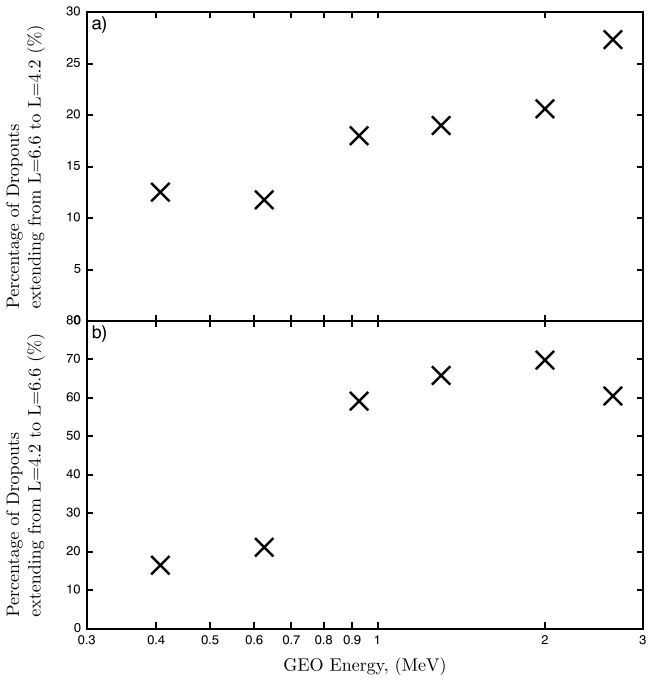

Figure 4. (a) Percentage of GEO dropouts extending to $L \sim 4.2$ at equivalent first adiabatic invariants. (b) Percentage of GPS dropouts at $L \sim 4.2$ extending up to GEO ($L = 6.6$) at equivalent first adiabatic invariants.

(Boynton, Mourenas, et al., 2016; Turner et al., 2013). Thus, dropouts on GPS orbit extending up to GEO should likely correspond to true losses as well.

A data set of electron flux dropouts at GEO ($L = 6.6$) previously identified by Boynton, Mourenas, et al. (2016) based on LANL satellite measurements has been employed to first evaluate the inward radial extension of relativistic electron PSD dropouts occurring at GEO, at fixed first adiabatic invariant. For each of the GEO dropouts at each energy, the dropouts at $L \sim 4.2$ were checked to identify any corresponding dropout occurring during the same time interval and with a similar first adiabatic invariant. Table 5 shows the energy channels for the GEO dropouts, together with the GPS energy channels at $L \sim 4.2$ corresponding to a similar first adiabatic invariant. The percentage of GEO dropouts extending down to GPS orbit was calculated for each GEO energy and plotted in Figure 4a, demonstrating that the proportion of fast and deep relativistic electron dropouts extending from $L \sim 6.6$ to $L \sim 4.2$ increases significantly with electron energy, climbing from 12% for 0.4–0.6 MeV at GEO (i.e., for 1–1.6 MeV at $L \sim 4.2$) to 20%–30% for 1–3 MeV at GEO (2–6 MeV at $L \sim 4.2$). Similarly, the percentage of GPS ($L \sim 4.2$) dropouts extending up to GEO was calculated for each GEO energy and plotted in Figure 4b, showing that 20% of the 1–1.6 MeV (energy at $L \sim 4.2$) GPS dropouts extend up to GEO, while ~60–70% of the 2–6 MeV (energy at $L \sim 4.2$) GPS dropouts extend to GEO.

This means that 25–40% of the multi-MeV GPS dropouts are localized around $L \sim 4.2$ and do not reach $L = 6.6$. Such dropouts (or at least a portion of them) might therefore correspond to fast precipitation induced by combined EMIC and whistler mode wave scattering localized in L. In addition, the 10 to 90 percentiles of the distribution of 3 MeV electron dropout magnitudes at $L \sim 4.2$ are sensibly higher for the subset of dropouts that do not extend up to GEO than for all the dropouts: the median magnitude, 80 and 90 percentiles for dropouts that do not extend up to GEO are 31, 489, 946, versus 27, 191, 664 for all the dropouts. Thus, multi-MeV dropouts localized around $L \sim 4.2$ are often stronger than dropouts extending up to GEO.

Conversely, many of the 60–70% of multi-MeV dropouts that extend to GEO are likely related to magnetopause shadowing combined with outward radial diffusion—although precipitation loss may affect their total magnitude—explaining the prevalence of the sole B_s as their main governing factor. Actually, the fact that B_s is the sole main governing factor for MeV dropouts at $L \sim 4.2$ stands in stark contrast with the results from a previous ERR analysis, which showed that both B_s and p are among the main governing terms for such dropouts at GEO (Boynton, Mourenas, et al., 2016). This implies that dynamic pressure impulses have a definitely weaker impact on dropouts occurring closer to the Earth as compared with southward IMF.

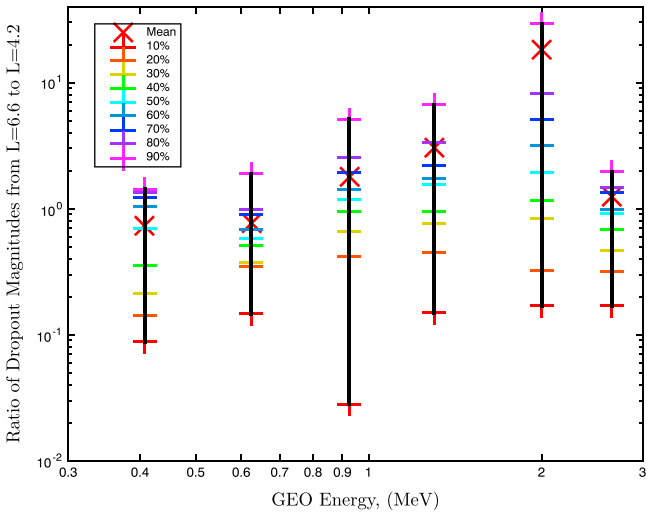

Figure 5. The ratio of GEO to $L \sim 4.2$ dropout magnitudes at equivalent first adiabatic invariants.

The ratio of GEO to GPS orbit dropout magnitudes was also calculated for each of the wide (in L) relativistic electron dropouts. The mean and the 10, 20, 30, 40, 50, 60, 70, 80, and 90 percentiles of this ratio are plotted in Figure 5, showing that both the mean and median ratios increase up to a GEO energy of 2 MeV and then decrease at 2.65 MeV, being generally comprised between 0.6 and 2. Figure 5 further shows that 40% to 60% of the relativistic electron dropouts at $L \sim 4.2$ are stronger than at $L = 6.6$ when they extend up to GEO. This could be due to either the presence of an additional loss process at GPS orbit compared with GEO, or to the initial L distribution of the PSD and the way the dropout develops from GEO, which may sometimes allow a stronger reduction at lower L.

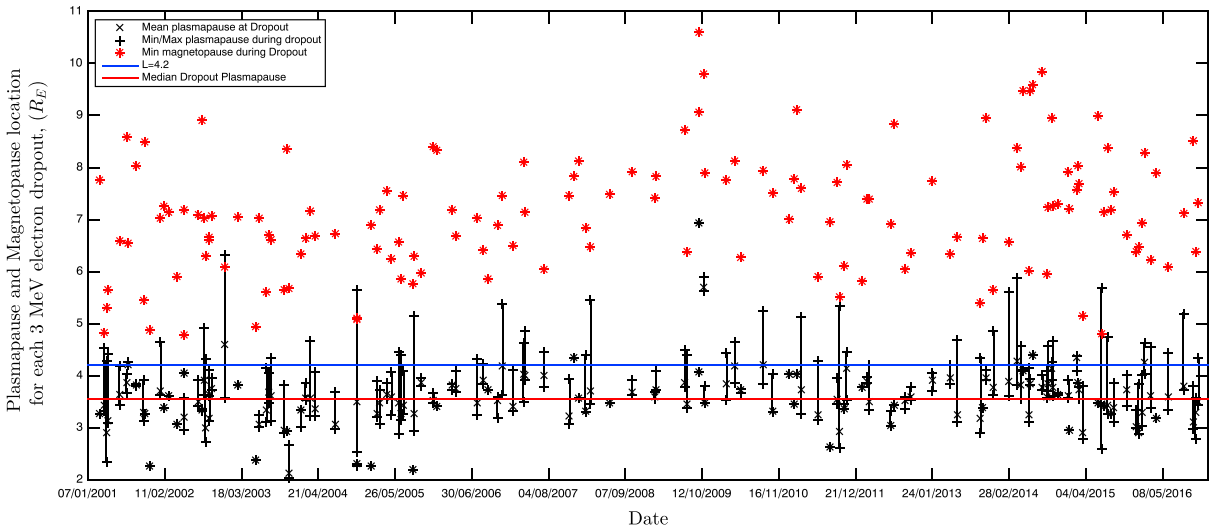

Figure 6. Plasmapause positions (black points) calculated from the *AE* index based on the statistical model from O'Brien and Moldwin (2003) versus $L \sim 4.2$ (indicated by a blue line), during GPS dropouts at 3 MeV. The median is also indicated (red line). The corresponding minimum magnetopause positions during dropouts, calculated via the Shue et al. (1998) model, are shown by red points.

6. GPS Dropout Occurrences Versus Plasmapause and Magnetopause Location

It is interesting to check the plasmapause position L_{pp} with respect to the GPS satellite (i.e., $L \sim 4.2$ here) during the dropouts, because of the known absence of hiss and chorus waves over a L range comprised between $\sim L_{pp}-0.5$ and $\sim L_{pp}+0.1$ (e.g., see Mourenas et al., 2017, and references therein). Strong precipitation-related dropouts should not occur there (in contrast, there is no such restriction concerning the presence of EMIC waves near $L \sim 4.2$). Moreover, chorus-induced acceleration of electrons up to MeVs generally occurs just above the plasmapause (Horne et al., 2005) and may facilitate the subsequent occurrence of multi-MeV dropouts by substantially increasing the flux levels there. One therefore expects that precipitation-related dropouts at $L \sim 4.2$ should correspond to $L_{pp} < 4.1$ or $L_{pp} > 4.7$. Figure 6 shows the position of the plasmapause calculated from the *AE* index based on the statistical plasmapause model from O'Brien and Moldwin (2003) versus $L \sim 4.2$, during dropouts at 3 MeV. The median L_{pp} location is also marked. During most 3 MeV electron dropouts, one indeed finds that $L_{pp} < 4$. In such a case, precipitation-induced dropouts should generally be ascribed to combined effects of EMIC and chorus waves, although hiss waves could also be present in duskside high-density plumes.

Finally, the minimum magnetopause locations during each 3 MeV dropout, calculated using the model of Shue et al. (1998), have also been plotted in Figure 6. For nearly 50% of the dropouts, the magnetopause remained above $L = 6.6$, while for roughly 20% of the dropouts, the magnetopause never reached L shells smaller than 8. Consequently, magnetopause shadowing was likely significant in at least half of these dropouts. However, results in Figure 6 suggest again that magnetopause shadowing was probably not the main cause for ~20% of the dropouts. This likely accounts, at least partially, for the weak dependence of MeV dropouts at $L \sim 4.2$ on solar wind dynamic pressure.

7. Conclusions

High-quality data from GPS satellites have been used to perform a statistical study of fast and strong electron flux dropouts that have occurred at $L \sim 4.2$ between 2001 and 2016. Such dropouts have been automatically selected and statistics of dropout magnitudes and occurrence rates as a function of electron energy (between 120 keV and 10 MeV) have been derived. The Error Reduction Ratio (ERR) analysis has been further used to identify possible linear and nonlinear relationships between dropouts and solar wind or geomagnetic activity indices.

The 1–10 MeV electron dropouts turn out to be both more frequent and stronger than dropouts at 120–800 keV. In particular, the mean magnitude of multi-MeV dropouts appears much larger than at lower

energy. The median dropout magnitude also increases with energy, although sensibly less rapidly. The ERR analysis shows the presence of a similar threshold in the main factors governing GPS dropouts. While both the southward IMF B_s, solar wind dynamic pressure p, and *Dst* index, can influence dropout magnitudes at low energy, B_s becomes by far the most important controlling factor above ~0.8–1 MeV, with no significant influence from dynamic pressure p or *Dst*. This contrasts with a previous ERR analysis at GEO, which showed that 1–3 MeV electron dropouts at $L = 6.6$ are controlled by both B_s and p (Boynton, Mourenas, et al., 2016). Moreover, we found that for ~20% of the multi-MeV electron dropouts at $L \sim 4.2$, the magnetopause remained above $L = 8$, while during 25–40 % of these dropouts at $L = 4.2$, no similar dropout was recorded at geostationary orbit. Taken as a whole, all these results are consistent with the presence of some additional loss mechanism at multi-MeV energy as compared with lower energies during many dropouts at $L \sim 4.2$, and they further indicate that this additional loss mechanism should depend principally on B_s and that it should be relatively independent of magnetopause shadowing. It therefore suggests an important role of precipitation loss due to combined EMIC and whistler mode waves in a significant fraction of these events. Such occasional precipitation losses would increase the mean magnitude of multi-MeV dropouts and more generally modulate dropout strength, supplementing magnetopause shadowing and outward radial diffusion that also affect dropouts at lower energies.

We found also that almost all multi-MeV electron dropouts at $L \sim 4.2$ occurred above the plasmapause. The present statistical results are therefore consistent with a significant contribution from precipitation induced by simultaneous EMIC and chorus waves in multi-MeV electron dropouts at $L \sim 4.2$. In the future, it would be useful to examine in more details in GPS data the magnetic local time development of each of these dropouts, to study the radial progression of dropouts at L shells comprised between $L \sim 4.2$ and $L = 6.6$, and to check the presence of EMIC and whistler mode waves from other available satellites: all this would help to confirm (or not) the proposed interpretation of the present results, but it is beyond the scope of the present paper. Finally, we note that a 12 h resolution data set was used in our analysis. This focus on dropouts lasting at least 12 h stems in part from our interest in time-integrated effects on satellites but also from the usefulness of averaging fluxes from various GPS satellites over half a day to get rid of spurious count variations. Moreover, dropouts of >1.1 MeV electrons driven by high-speed streams were found to last >18–24 h at geostationary orbit (Borovsky & Denton, 2009). Studies of other dropouts give similar time scales in the outer belt and show that it takes generally more time to recover initial flux levels for multi-MeV dropouts (e.g., Turner, Angelopoulos, Li, et al., 2014). Nevertheless, dropouts of <500 keV electrons may last less than that, due to substorm-related injections (e.g., Turner, Angelopoulos, Li, et al., 2014).Therefore, some fast and very short-lived dropouts, lasting less than 12 h due to a very fast recovery of electron flux levels in less than half a day, might not be identified. Such very short-lived dropouts would be worth examining too in future work.

Acknowledgments
We gratefully acknowledge the CXD team at Los Alamos National Laboratory which designed and built the CXD and BDD-IIR GPS instruments over more than 20 years. The LANL-GPS electron flux data are supplied by NOAA (https://www.ngdc.noaa.gov/stp/space-weather/satellite-data/satellite-systems/gps/), while the solar wind and geomagnetic indices were supplied by OMNIweb (http://omniweb.gsfc.nasa.gov). The work was performed within the project Rad-Sat and has received financial support from the UK Natural Environment Research Council (NERC) [10.13039/501100000270] under grant NE/P017061/1. Part of the research done has received funding from and the European Union Horizon 2020 Research and Innovation programme under grant agreement 637302 PROGRESS.

References

Arnoldy, R. L. (1971). Signature in the interplanetary medium for substorms. *Journal of Geophysical Research*, *76*(22), 5189–5201.

Artemyev, A., Agapitov, O., Mourenas, D., Krasnoselskikh, V., Shastun, V., & Mozer, F. (2016). Oblique whistler-mode waves in the Earths inner magnetosphere: Energy distribution, origins, and role in radiation belt dynamics. *Space Science Reviews*, *200*(1), 261–355.

Artemyev, A. V., Orlova, K. G., Mourenas, D., Agapitov, O. V., & Krasnoselskikh, V. V. (2013). Electron pitch-angle diffusion: Resonant scattering by waves vs. nonadiabatic effects. *Annales de Geophysique*, *31*(9), 1485–1490.

Bailey, D. K. (1968). Some quantitative aspects of electron precipitation in and near the auroral zone. *Reviews of Geophysics*, *6*(3), 289–346.

Baker, D. N., Blake, J. B., Klebesadel, R. W., & Higbie, P. R. (1986). Highly relativistic electrons in the Earth's outer magnetosphere: 1. Lifetimes and temporal history 1979–1984. *Journal of Geophysical Research*, *91*(A4), 4265–4276.

Balikhin, M. A., Boynton, R. J., Billings, S. A., Gedalin, M., Ganushkina, N., Coca, D., & Wei, H. (2010). Data based quest for solar wind-magnetosphere coupling function. *Geophysical Research Letters*, *37*, L24107. https://doi.org/10.1029/2010GL045733

Balikhin, M. A., Gedalin, M., Reeves, G. D., Boynton, R. J., & Billings, S. A. (2012). Time scaling of the electron flux increase at GEO: The local energy diffusion model vs observations. *Journal of Geophysical Research*, *117*, A10208. https://doi.org/10.1029/2012JA018114

Balikhin, M. A., Shprits, Y. Y., Walker, S. N., Chen, L., Cornilleau-Wehrlin, N., Dandouras, I., … Weiss, B. (2015). Observations of discrete harmonics emerging from equatorial noise. *Nature Communications*, *6*, 7703. https://doi.org/10.1038/ncomms8703

Billings, S., Korenberg, M., & Chen, S. (1988). Identification of non-linear output affine systems using an orthogonal least-squares algorithm. *International Journal of Systems Science*, *19*, 1559–1568.

Borovsky, J. E., & Denton, M. H. (2009). Relativistic-electron dropouts and recovery: A superposed epoch study of the magnetosphere and the solar wind. *Journal of Geophysical Research*, *114*, A02201. https://doi.org/10.1029/2008JA013128

Borovsky, J. E., & Denton, M. H. (2010). Magnetic field at geosynchronous orbit during high-speed stream-driven storms: Connections to the solar wind, the plasma sheet, and the outer electron radiation belt. *Journal of Geophysical Research*, *115*, A08217. https://doi.org/10.1029/2009JA015116

Bortnik, J., Thorne, R. M., O'Brien, T. P., Green, J. C., Strangeway, R. J., Shprits, Y. Y., & Baker, D. N. (2006). Observation of two distinct, rapid loss mechanisms during the 20 November 2003 radiation belt dropout event. *Journal of Geophysical Research*, *111*, A12216. https://doi.org/10.1029/2006JA011802

Boynton, R. J., Balikhin, M. A., Billings, S. A., Reeves, G. D., Ganushkina, N., Gedalin, M., … Walker, S. N. (2013). The analysis of electron fluxes at geosynchronous orbit employing a NARMAX approach. *Journal of Geophysical Research: Space Physics*, *118*, 1500–1513. https://doi.org/0.1002/jgra.50192

Boynton, R. J., Balikhin, M. A., Billings, S. A., Sharma, A. S., & Amariutei, O. A. (2011). Data derived NARMAX *Dst* model. *Annales Geophysicae*, *29*(6), 965–971. https://doi.org/10.5194/angeo-29-965-2011

Boynton, R. J., Balikhin, M. A., Billings, S. A., Wei, H. L., & Ganushkina, N. (2011). Using the NARMAX OLS-ERR algorithm to obtain the most influential coupling functions that affect the evolution of the magnetosphere. *Journal of Geophysical Research*, *116*, A05218. https://doi.org/10.1029/2010JA015505

Boynton, R. J., Balikhin, M. A., & Billings, S. A. (2015). Online NARMAX model for electron fluxes at GEO. *Annales de Geophysique*, *33*(3), 405–411.

Boynton, R. J., Balikhin, M. A., & Mourenas, D. (2014). Statistical analysis of electron lifetimes at GEO: Comparisons with chorus-driven losses. *Journal of Geophysical Research: Space Physics*, *119*, 6356–6366. https://doi.org/10.1002/2014JA019920

Boynton, R. J., Balikhin, M. A., Sibeck, D. G., Walker, S. N., Billings, S. A., & Ganushkina, N. (2016). Electron flux models for different energies at geostationary orbit. *Space Weather*, *14*, 846–860. https://doi.org/10.1002/2016SW001506

Boynton, R. J., Mourenas, D., & Balikhin, M. A. (2016). Electron flux dropouts at geostationary earth orbit: Occurrences, magnitudes, and main driving factors. *Journal of Geophysical Research: Space Physics*, *121*, 8448–8461. https://doi.org/10.1002/2016JA022916

Dessler, A. J., & Karplus, R. (1961). Some effects of diamagnetic ring currents on Van Allen radiation. *Journal of Geophysical Research*, *66*(8), 2289–2295.

Gao, X., Li, W., Bortnik, J., Thorne, R. M., Lu, Q., Ma, Q., … Wang, S. (2015). The effect of different solar wind parameters upon significant relativistic electron flux dropouts in the magnetosphere. *Journal of Geophysical Research: Space Physics*, *120*, 4324–4337. https://doi.org/10.1002/2015JA021182

Green, J. C., Onsager, T. G., O'Brien, T. P., & Baker, D. N. (2004). Testing loss mechanisms capable of rapidly depleting relativistic electron flux in the Earth's outer radiation belt. *Journal of Geophysical Research*, *109*, A12211. https://doi.org/10.1029/2004JA010579

Horne, R. B., Thorne, R. M., Shprits, Y. Y., Meredith, N. P., Glauert, S. A., Smith, A. J., … Decreau, P. M. E. (2005). Wave acceleration of electrons in the Van Allen radiation belts. *Nature*, *437*(7056), 227–230.

Kersten, T., Horne, R. B., Glauert, S. A., Meredith, N. P., Fraser, B. J., & Grew, R. S. (2014). Electron losses from the radiation belts caused by EMIC waves. *Journal of Geophysical Research: Space Physics*, *119*, 8820–8837. https://doi.org/10.1002/2014JA020366

Kim, H.-J., & Chan, A. A. (1997). Fully adiabatic changes in storm time relativistic electron fluxes. *Journal of Geophysical Research*, *102*(A10), 22,107–22,116.

Kim, K.-C., & Lee, D.-Y. (2014). Magnetopause structure favorable for radiation belt electron loss. *Journal of Geophysical Research: Space Physics*, *119*, 5495–5508. https://doi.org/10.1002/2014JA019880

Kim, K. C., Lee, D.-Y., Kim, H.-J., Lyons, L. R., Lee, E. S., Öztürk, M. K., & Choi, C. R. (2008). Numerical calculations of relativistic electron drift loss effect. *Journal of Geophysical Research*, *113*, A09212. https://doi.org/10.1029/2007JA013011

Li, X., Baker, D. N., Zhao, H., Zhang, K., Jaynes, A. N., Schiller, Q., … Temerin, M. (2017). Radiation belt electron dynamics at low l (<4): Van Allen Probes era versus previous two solar cycles. *Journal of Geophysical Research: Space Physics*, *122*, 5224–5234. https://doi.org/10.1002/2017JA023924

Li, W., Shprits, Y. Y., & Thorne, R. M. (2007). Dynamic evolution of energetic outer zone electrons due to wave-particle interactions during storms. *Journal of Geophysical Research*, *112*, A10220. https://doi.org/10.1029/ 2007JA012368

Lorentzen, K. R., Looper, M. D., & Blake, J. B. (2001). Relativistic electron microbursts during the GEM storms. *Geophysical Research Letters*, *28*(13), 2573–2576.

Mann, I. R., Ozeke, L. G., Murphy, K. R., Claudepierre, S. G., Turner, D. L., Baker, D. N., … Honary, F. (2016). Explaining the dynamics of the ultra-relativistic third Van Allen radiation belt. *Nature Physics*, *12*(10), 978–983.

McIlwain, C. E. (1966). Ring current effects on trapped particles. *Journal of Geophysical Research*, *71*(15), 3623–3628.

Meng, C. I., Tsurutani, B., Kawasaki, K., & Akasofu, S. I. (1973). Cross-correlation analysis of the *AE* index and the interplanetary magnetic field B_z component. *Journal of Geophysical Research*, *78*(4), 617–629.

Meredith, N. P., Horne, R. B., Glauert, S. A., & Anderson, R. R. (2007). Slot region electron loss timescales due to plasmaspheric hiss and lightning-generated whistlers. *Journal of Geophysical Research*, *112*, A08214. https://doi.org/10.1029/2007JA012413

Meredith, N. P., Horne, R. B., Glauert, S. A., Thorne, R. M., Summers, D., Albert, J. M., & Anderson, R. R. (2006). Energetic outer zone electron loss timescales during low geomagnetic activity. *Journal of Geophysical Research*, *111*, A05212. https://doi.org/10.1029/2005JA011516

Meredith, N. P., Horne, R. B., Kersten, T., Fraser, B. J., & Grew, R. S. (2014). Global morphology and spectral properties of EMIC waves derived from CRRES observations. *Journal of Geophysical Research: Space Physics*, *119*, 5328–5342. https://doi.org/10.1002/2014JA020064

Morley, S. K., Sullivan, J. P., Carver, M. R., Kippen, R. M., Friedel, R. H. W., Reeves, G. D., & Henderson, M. G. (2017). Energetic particle data from the global positioning system constellation. *Space Weather*, *15*, 283–289. https://doi.org/10.1002/2017SW001604

Morley, S. K., Sullivan, J. P., Henderson, M. G., Blake, J. B., & Baker, D. N. (2016). The Global Positioning System constellation as a space weather monitor: Comparison of electron measurements with Van Allen Probes data. *Space Weather*, *14*, 76–92. https://doi.org/10.1002/2015SW001339

Mourenas, D., Artemyev, A. V., Agapitov, O. V., & Krasnoselskikh, V. (2013). Analytical estimates of electron quasi-linear diffusion by fast magnetosonic waves. *Journal of Geophysical Research: Space Physics*, *118*, 3096–3112. https://doi.org/10.1002/jgra.50349

Mourenas, D., Artemyev, A. V., Agapitov, O. V., & Krasnoselskikh, V. (2014). Consequences of geomagnetic activity on energization and loss of radiation belt electrons by oblique chorus waves. *Journal of Geophysical Research: Space Physics*, *119*, 2775–2796. https://doi.org/10.1002/2013JA019674

Mourenas, D., Artemyev, A. V., Ma, Q., Agapitov, O. V., & Li, W. (2016). Fast dropouts of multi-MeV electrons due to combined effects of EMIC and whistler mode waves. *Geophysical Research Letters*, *43*, 4155–4163. https://doi.org/10.1002/2016GL068921

Mourenas, D., Ma, Q., Artemyev, A. V., & Li, W. (2017). Scaling laws for the inner structure of the radiation belts. *Geophysical Research Letters*, *44*, 3009Ű3018. https://doi.org/10.1002/2017GL072987

Mourenas, D., Artemyev, A. V., Ripoll, J.-F., Agapitov, O. V., & Krasnoselskikh, V. V. (2012). Timescales for electron quasi-linear diffusion by parallel and oblique lower-band chorus waves. *Journal of Geophysical Research*, *117*, A06234. https://doi.org/10.1029/2012JA017717

O'Brien, T. P., & Moldwin, M. B. (2003). Empirical plasmapause models from magnetic indices. *Geophysical Research Letters*, *30*(4), 1152. https://doi.org/10.1029/2002GL016007

Orlova, K., & Shprits, Y. (2014). Model of lifetimes of the outer radiation belt electrons in a realistic magnetic field using realistic chorus wave parameters. *Journal of Geophysical Research: Space Physics*, *119*, 770–780. https://doi.org/10.1002/2013JA019596

Ozeke, L. G., Mann, I. R., Murphy, K. R., Jonathan Rae, I., & Milling, D. K. (2014). Analytic expressions for ULF wave radiation belt radial diffusion coefficients. *Journal of Geophysical Research: Space Physics*, *119*, 1587–1605. https://doi.org/10.1002/2013JA019204

Ozturk, M. K., & Wolf, R. A. (2007). Bifurcation of drift shells near the dayside magnetopause. *Journal of Geophysical Research*, *112*, A07207. https://doi.org/10.1029/2006JA012102

Sergeev, V., & Tsyganenko, N. (1982). Energetic particle losses and trapping boundaries as deduced from calculations with a realistic magnetic field model. *Planetary and Space Science*, *30*(10), 999–1006.

Shprits, Y. Y., Thorne, R. M., Friedel, R., Reeves, G. D., Fennell, J., Baker, D. N., & Kanekal, S. G. (2006). Outward radial diffusion driven by losses at magnetopause. *Journal of Geophysical Research*, *111*, A11214. https://doi.org/10.1029/2006JA011657

Shue, J.-H., Song, P., Russell, C. T., Steinberg, J. T., Chao, J. K., Zastenker, G., … Kawano, H. (1998). Magnetopause location under extreme solar wind conditions. *Journal of Geophysical Research*, *103*(A8), 17,691–17,700.

Su, Z., Gao, Z., Zhu, H., Li, W., Zheng, H., Wang, Y., … Wygant, J. R. (2016). Nonstorm time dropout of radiation belt electron fluxes on 24 September 2013. *Journal of Geophysical Research: Space Physics*, *121*, 6400–6416. https://doi.org/10.1002/2016JA022546

Summers, D., & Thorne, R. M. (2003). Relativistic electron pitch-angle scattering by electromagnetic ion cyclotron waves during geomagnetic storms. *Journal of Geophysical Research*, *108*(A4), 1143. https://doi.org/10.1029/2002JA009489

Turner, D. L., Angelopoulos, V., Li, W., Bortnik, J., Ni, B., Ma, Q., … Rodriguez, J. V. (2014). Competing source and loss mechanisms due to wave-particle interactions in Earth's outer radiation belt during the 30 September to 3 October 2012 geomagnetic storm. *Journal of Geophysical Research: Space Physics*, *119*, 1960–1979. https://doi.org/10.1002/2014JA019770

Turner, D. L., Angelopoulos, V., Morley, S. K., Henderson, M. G., Reeves, G. D., Li, W., … Rodriguez, J. V. (2014). On the cause and extent of outer radiation belt losses during the 30 September 2012 dropout event. *Journal of Geophysical Research: Space Physics*, *119*, 1530–1540. https://doi.org/10.1002/2013JA019446

Turner, D. L., Morley, S. K., Miyoshi, Y., Ni, B., & Huang, C.-L. (2013). Outer radiation belt flux dropouts: Current understanding and unresolved questions. In Summers, D., Mann, I. R., Baker, D. N., & Schulz, M. (Eds.), *Dynamics of the Earth's radiation belts and inner magnetosphere* (Vol. 199, pp. 195–212). Washington, DC: American Geophysical Union. https://doi.org/10.1029/2012GM001310

Turner, D. L., O'Brien, T. P., Fennell, J. F., Claudepierre, S. G., Blake, J. B., Jaynes, A. N., … Reeves, G. D. (2017). Investigating the source of near-relativistic and relativistic electrons in Earth's inner radiation belt. *Journal of Geophysical Research: Space Physics*, *122*, 695–710. https://doi.org/10.1002/2016JA023600

Turner, D. L., Shprits, Y., Hartinger, M., & Angelopoulos, V. (2012). Explaining sudden losses of outer radiation belt electrons during geomagnetic storms. *Nature Physics*, *8*(3), 208–212.

Ukhorskiy, A. Y., Sitnov, M. I., Millan, R. M., Kress, B. T., Fennell, J. F., Claudepierre, S. G., & Barnes, R. J. (2015). Global storm time depletion of the outer electron belt. *Journal of Geophysical Research: Space Physics*, *120*, 2543–2556. https://doi.org/10.1002/2014JA020645

Usanova, M. E., & Mann, I. R. (2016). *Understanding the role of EMIC waves in radiation belt and ring current dynamics: Recent advances in waves, particles, and storms in geospace: A complex interplay*. Oxford: Oxford University Press.

Welling, D. (2010). The long-term effects of space weather on satellite operations. *Annales de Geophysique*, *28*(6), 1361–1367.

Wrenn, G. L. (1995). Conclusive evidence for internal dielectric charging anomalies on geosynchronous communications spacecraft. *Journal of Spacecraft and Rockets*, *32*(3), 514–520.

Yuan, C., & Zong, Q. (2013). Relativistic electron fluxes dropout in the outer radiation belt under different solar wind conditions. *Journal of Geophysical Research: Space Physics*, *118*, 7545–7556. https://doi.org/10.1002/2013JA019066

Zhang, X.-J., Li, W., Thorne, R. M., Angelopoulos, V., Bortnik, J., Kletzing, C. A., … Hospodarsky, G. B. (2016). Statistical distribution of EMIC wave spectra: Observations from Van Allen Probes. *Geophysical Research Letters*, *43*, 12,348–12,355. https://doi.org/10.1002/2016GL071158

Zhang, X.-J., Mourenas, D., Artemyev, A. V., Angelopoulos, V., & Thorne, R. M. (2017). Contemporaneous EMIC and whistler mode waves: Observations and consequences for MeV electron loss. *Geophysical Research Letters*, *44*, 8113–8121. https://doi.org/10.1002/2017GL073886